Downloaded from orbit.dtu.dk on: Mar 20, 2025

DTU Library

Charging of carbon thin films in scanning and phase-plate transmission electron microscopy

Hettler, Simon; Kano, Emi; Dries, Manuel; Gerthsen, Dagmar; Pfaffmann, Lukas; Bruns, Michael; Beleggia, Marco; Malac, Marek

Published in:
Ultramicroscopy

Link to article, DOI:
10.1016/j.ultramic.2017.09.009

Publication date:
2018

Document Version
Peer reviewed version

Link back to DTU Orbit

Citation (APA):
Hettler, S., Kano, E., Dries, M., Gerthsen, D., Pfaffmann, L., Bruns, M., Beleggia, M., & Malac, M. (2018). Charging of carbon thin films in scanning and phase-plate transmission electron microscopy. *Ultramicroscopy*, *184*, 252-266. https://doi.org/10.1016/j.ultramic.2017.09.009

General rights
Copyright and moral rights for the publications made accessible in the public portal are retained by the authors and/or other copyright owners and it is a condition of accessing publications that users recognise and abide by the legal requirements associated with these rights.

- Users may download and print one copy of any publication from the public portal for the purpose of private study or research.
- You may not further distribute the material or use it for any profit-making activity or commercial gain
- You may freely distribute the URL identifying the publication in the public portal

If you believe that this document breaches copyright please contact us providing details, and we will remove access to the work immediately and investigate your claim.

ACCEPTED MANUSCRIPT

Charging of carbon thin films in scanning and phase-plate transmission electron microscopy

Simon Hettler[a,*], Emi Kano[b], Manuel Dries[a], Dagmar Gerthsen[a], Lukas Pfaffmann[c], Michael Bruns[c], Marco Beleggia[d], Marek Malac[b]

[a]*Laboratory for Electron Microscopy, Karlsruhe Institute of Technology, Engesserstrasse 7, 76131 Karlsruhe, Germany*
[b]*National Institute for Nanotechnology and Deptartment of Physics, University of Alberta, 11421 Saskatchewan Drive, Edmonton, T6G 2M9, Canada*
[c]*Institute for Applied Materials - Energy Storage Systems, Karlsruhe Institute of Technology, Hermann-von-Helmholtz-Platz 1, 76344 Eggenstein-Leopoldshafen, Germany*
[d]*Center for Electron Nanoscopy, Technical University of Denmark, DK-2800 Kgs. Lyngby, Denmark*

Abstract

A systematic study on charging of carbon thin films under intense electron-beam irradiation was performed in a transmission electron microscope to identify the underlying physics for the functionality of hole-free phase plates. Thin amorphous carbon films fabricated by different deposition techniques and single-layer graphene were studied. Clean thin films at moderate temperatures show small negative charging while thin films kept at an elevated temperature are stable and not prone to beam-generated charging. The charging is attributed to electron-stimulated desorption (ESD) of chemisorbed water molecules from the thin-film surfaces and an accompanying change of work function. The ESD interpretation is supported by experimental results obtained by electron-energy loss spectroscopy, hole-free phase plate imaging, secondary electron detection and x-ray photoelectron spectroscopy as well as simulations of the electrostatic potential distribution. The described ESD-based model explains previous experimental findings and is of general interest to any phase-related technique in a transmission electron microscope.

Keywords: scanning transmission electron microscopy, transmission electron microscopy, electron-beam induced charging, thin film, phase plate, radiation damage, hole-free phase plate, Volta phase plate

1. Introduction

Charging of insulating specimens is a well-known issue in electron microscopy, including transmission (TEM), scanning TEM (STEM) and scanning electron microscopy (SEM) and can lead to severe image degradation and sample damage. The charging effect is pronounced in cryo (S)TEM and SEM applications because the electrical conductivity of typical biological samples is very low at liquid nitrogen temperature [1]. Although a thin layer of amorphous carbon (aC) is typically sufficient to reduce charging effects to an acceptable level, it turns out that aC films are prone to charging themselves, commonly referred to as the ”Berriman effect” [2]. This led

*Corresponding author: simon.hettler@kit.edu

ACCEPTED MANUSCRIPT

to a search for an optimal specimen support for cryo applications and other means of reducing specimen charging [3–5]. The origin of most charging effects is the generation of secondary electrons (SEs) which escape from the specimen and leave positively charged ions behind [6–8]. For insulating materials, the electrostatic charging remains even at elevated temperatures and affects the electron beam leading to severe image degradation. If the electrical conductivity of the specimen is sufficiently high, the charge is compensated by a current from ground and observable charging should not be present. However, charging effects were observed on aC, a material which is assumed to have sufficient electrical conductivity [2]. Proposed explanations are that the surface of the aC layer has insulating properties or that charging occurs in a contamination layer adsorbed on the aC film [9, 10].

Only recently, the charging of aC thin films has found a beneficial application in the use as hole-free phase plate (PP) for TEM [8]. PPs increase the image contrast of electron-transparent objects by inducing a phase shift between the unscattered and scattered part of the electron wave in the back focal plane (BFP) of the objective lens [11–13]. The charging of aC films is exploited by placing a uniform thin film in the BFP on which a charged area is created by the intense zero-order beam of unscattered electrons causing the desired phase shift. This concept of the hole-free (HF) PP has overcome several limitations of previous PP approaches [8]. Interestingly, both polarities of the charged area, positive and negative, have been reported in the literature [8, 14, 15]. While positive charging can be well explained by an insulating surface of the aC film, the physical reason for negative charging is still not understood.

In the present study, we systematically analyzed three aC thin films fabricated by different evaporation devices and a single-layer graphene (SLG) sample in a transmission electron microscope to identify the physical reasons for the charging of C thin films. We performed electron-energy loss spectroscopy (EELS) and HFPP imaging at different thin-film temperatures yielding the trace of the film thickness and a measure for phase shift arising from a change in the film thickness and from possible charging of the thin film. To separate charging from contamination effects, different steps were undertaken to avoid contamination of the thin films [16]. X-ray photoelectron spectroscopy (XPS) data provides additional information on the chemical composition of the thin film surfaces. The experimental results indicate that charging of *clean* C thin films is small, has a negative polarity and its magnitude decreases with increasing temperature. The negative polarity of the charge is explained by a local change in the work function (WF) induced by electron-stimulated desorption (ESD) of chemisorbed molecules on the thin-film surface which is supported by simulations of the electrostatic potential. This effect also describes the functionality of HFPPs with negative polarity [14] and is of general interest to any phase-related technique in a transmission electron microscope.

2. Materials and methods

We used the identical methods to analyze the phase-plate films, referred to as *thin films* in the following, as in our recent publication [16]. TEM experiments were performed in a dry-pumped Hitachi HF-3300 transmission electron microscope (Hitachi High Technologies, Naka, Japan) with a cold field emission gun operated at 300 kV. The free-lens mode was used to set up the electron optics in order that the BFP of an additional test specimen placed in the condenser-lens system coincides with the standard object plane (Figure 1). For the collection of a time series of EELS spectra with a Gatan Image Filter (GIF Tridiem model 863, Gatan Inc., Pleasanton, CA, USA) the test specimen, a standard carbon replica sample with a 2160 lines/mm gold diffraction grating (Ted Pella, prod. no 607), was retracted to measure solely the electron-beam induced

thickness change of the thin film. The time evolution of the SE emission current from the thin film is acquired simultaneously with the time evolution of EELS spectra. For acquisition of HFPP image series using a Gatan Ultrascan 1000 camera (Gatan Inc.), the test specimen is inserted. The microscope was kept at pressures below $6 \cdot 10^{-8}$ mbar during the experiments. The total electron beam current was measured for each time series by a calibrated acquisition of an image of the probe and varied between 50 and 100 pA. In this electron-optical setup, the camera length is in the order of L=3 mm and the beam diameter on the thin film was ≈20 nm. The MAESTRO central computer control system for the electron microscopy laboratory was used for data acquisition [17].

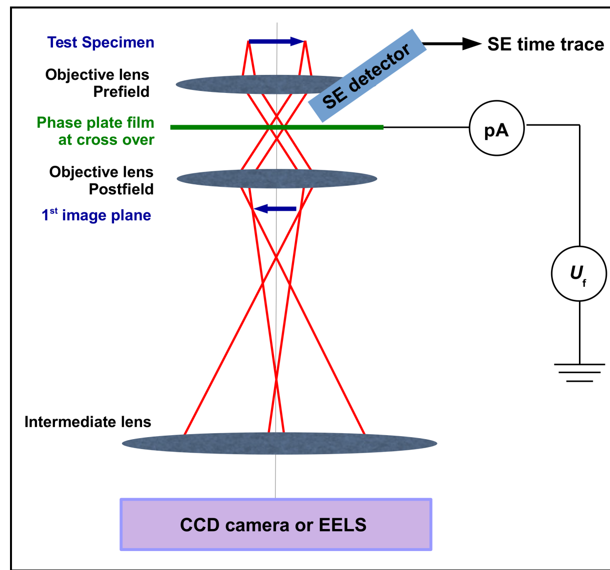

Figure 1: Schematic illustration of the electron-optical setup used to study charging of carbon thin films. An additional test specimen is implemented in an aperture holder above the objective lens. The tested phase-plate film is inserted in the sample holder plane that coincides with the BFP of the objective lens prefield. This allows to rapidly change the thin films and to heat the film or measure the return current to ground by using appropriate TEM holders. The imaging lenses can be adjusted for either EELS measurements or HFPP imaging. A SE detector is used to simultaneously record the SE time evolution with the EELS signal. Reprinted from [16] with permission.

EELS and HFPP data give information on changes of the thin-film thickness and on charging processes. The acquired low-loss (LL) EELS spectra allow the determination of the thickness evolution of the thin film by calculating

$$\frac{t}{\lambda} = log(\frac{I_{LL} + I_{ZL}}{I_{ZL}}) \quad (1)$$

with the intensity of the zero-loss peak I_{ZL}, the intensity of the LL region I_{LL}, the thin-film thickness t and the inelastic mean free path λ [18].

The power spectrum of a HFPP TEM image contains information on a phase shift caused by an electron-beam induced modification of the thin film. The Thon rings in power spectra of phase-contrast TEM images can be described by the phase-contrast transfer function (PCTF). Due to the low magnification achievable in this electron-optical setup, strong overfocus (-) values of Δf between 100 and 500 μm were used to ensure a good visibility of Thon-rings. The

ACCEPTED MANUSCRIPT

73 intermediate lens is used for defocusing. The effect of spherical aberration can be neglected for
74 the high defocus values leading to the PCTF [19]

$$PCTF \propto sin(-\pi \cdot \Delta f \cdot \lambda_e \cdot q^2 + \phi_{PP}) \tag{2}$$

75 with the electron wavelength λ_e and the spatial frequency q. ϕ_{PP} is the phase shift of the
76 unscattered electrons ($q = 0$) relative to the scattered electrons ($q > 0$) caused by charging of the
77 thin film. In this convention, a positively charged patch on the thin film implies a positive value
78 for ϕ_{PP}. Detailed information on the determination of the charge polarity can be found in [15].

79 The phase shift ϕ_{PP} and defocus Δf of the images are determined by a Matlab-based (Math-
80 Works, Natick, MA, USA) pattern recognition software [20] under the assumption that the phase
81 shift is only induced on the unscattered electrons. A time series of HFPP TEM images allows
82 to trace the PCTF evolution and thus the phase shift induced by an electron-beam induced mod-
83 ification of the thin film. As the PCTF appears squared in the power spectra, a phase shift of
84 π between two power spectra cannot be distinguished. This implies that the sign of phase shift
85 steps between subsequent power spectra of close to $\pi/2$ is ambiguous.

86 The XPS analysis was performed using a K-Alpha$^+$ spectrometer (Thermo Fisher Scientific,
87 Waltham, MA, USA) equipped with an Al-K_α source (1486.6 eV) and a 400 μm sized X-Ray
88 probe. Surface sputtering with 8 keV Ar clusters (2000 atoms, 4 eV per atom) was carried out to
89 clean the thin films from contamination and to study the actual thin-film properties. An electron
90 flood gun was used to compensate charging of the thin film during the measurement. Data
91 analysis and quantification of the bond structures was performed using the Avantage software
92 (Thermo Fisher Scientific).

93 Table 1 gives an overview over the investigated C thin films and their labeling within this
94 article. The PVD, EB and Thread aC thin films were fabricated by evaporation of a thin layer
95 on a freshly cleaved mica substrate (Plano, Wetzlar, Germany; Part No. 54) and were transfered
96 to Cu grids (Plano; Part No. G2150C/G2300C) in a subsequent floating process. Electron-beam
97 evaporation (EBE) was used to deposit the PVD aC and EB aC thin films using the PVD 75 (Kurt
98 J. Lesker Company, Hastings, UK) for the PVD aC thin film. The EB aC thin film was provided
99 by Michael Marko (Wadsworth Centre, New York State University, Albany, NY, USA) and was
100 fabricated with the Leica MED020 (Leica Microsystems, Wetzlar, Germany). The Thread aC
101 thin film was evaporated using a custom-built carbon-thread evaporation system. The thickness
102 of the PVD and Thread aC thin film was measured by TEM analysis of a cross-section TEM
103 specimen prepared by focused-ion-beam milling from a simultaneously coated Si wafer. The
104 thickness of the EB aC thin film was measured during the evaporation process with a crystal
105 thickness monitor. The thin films on their supporting grids were kept in clean plastic boxes for
106 a longer time period prior to transfer into the electron microscope. The single-layer graphene
107 (SLG) sample was grown on a Cu foil by chemical vapor deposition and then transferred to
108 TEM grids using a previously described method [21]. We used gold TEM grids covered with
109 an amorphous carbon film with 2 μm diameter holes (Quantifoil, Quantifoil Micro Tools GmbH,
110 Jena, Germany).

111 To avoid contamination, the thin films were cleaned by different methods as noted in Table 1.
112 UV cleaning [22] was carried out ex-situ using a 10 min cleaning procedure in the ZONE Cleaner
113 (Hitachi High Technologies Canada) for each side of the thin film. Heating of the thin films was
114 performed in situ and overnight at a temperature of >250 °C using a Gatan heating holder (Gatan
115 Inc.). Beam shower was performed by illuminating a large area around the region of interest with
116 a spread 300 keV beam with total areal doses $< 0.15 \frac{C}{cm^2}$. A Ronchigram was utilized to ensure

ACCEPTED MANUSCRIPT

Label	Preparation	Thickness	Cleaning procedure
PVD aC	EBE in Lesker PVD 75	10 nm	UV / heating
EB aC	EBE in Leica MED20	12 nm	heating
Thread aC	carbon-thread evaporation	5 - 7 nm	heating
SLG	Single-layer graphene	-	beam shower / heating

Table 1: List of analyzed C thin films.

117 that the BFP coincides with the thin film [23]. Multiple data collection runs were performed on
118 each thin film and experimental condition, such as the thin-film temperature. Each experimental
119 run was performed on a fresh area of the thin film.

120 3. Experimental Results

121 In this section we present the experimental results on thickness, SE and phase shift evolution
122 obtained by EELS and HFPP imaging. Subsequently, we show XPS measurements performed
123 on the PVD aC and EB aC thin films before presenting an analysis of previously published HFPP
124 image series.

125 *3.1. Evolution of the relative thickness*

126 Tracing the relative thickness (t/λ) evolution reveals processes linked to a deposition or re-
127 moval of material. Figure 2 shows exemplary t/λ evolutions for the three aC and the SLG thin
128 films in dependence of the areal electron dose. The time axes at the top of Figure 2 and in the
129 following Figures are calculated for an electron beam current of 60 pA and is for illustration
130 purposes only. The corresponding TEM images of the thin films acquired at a strong overfocus
131 (< - 1 mm) after the experimental series are displayed in Figure 3. The Thread aC thin film was
132 heated in situ for 2 nights at 275 °C to inhibit contamination and the PVD aC was cleaned in a UV
133 cleaning step prior to inserting it in the microscope. After either of the two cleaning procedures,
134 the thin films show a flat t/λ evolution indicating that there is neither hole-drilling nor contami-
135 nation (solid black and blue lines in Figure 2a). If the thin film is kept at room temperature (RT)
136 *in* the microscope for a few hours, contamination can recur as observable by the increasing t/λ
137 curve for the Thread aC thin film (dashed blue line in Figure 2a). While the electron beam does
138 not leave a visible mark on the UV cleaned PVD aC at RT and the Thread aC thin film at 300 °C
139 (Figure 3e and f), the contamination spot is clearly visible as a bright spot in Figure 3g for the
140 Thread aC kept at RT for 2.5 h due to the strong overfocus. Slight mechanical drift of the thin
141 film during data acquisition can be recognized as a minor elongation of the spot.
142 A different behavior is observed for the EB aC thin film. If the thin film is inserted in the
143 microscope without prior cleaning step and directly heated to 260 °C, the t/λ curve shows a
144 strong initial decrease followed by a slower increase (solid red line in Figure 2b). A TEM image
145 taken directly after the initial decrease reveals a slightly bright area surrounded by a darker ring
146 and a bright halo (Figure 3c) whereas the image taken at the end of the measurement reveals a
147 strong bright spot with dark halo indicating the deposition of contamination. Heating the EB aC
148 thin film in situ at 260 °C overnight leads to a strong decrease in the initial t/λ value from ≈
149 0.2 on the first day (solid red line) to 0.08 on the 2nd day (dotted red line) followed by a minor
150 decrease to 0.07 upon electron-beam illumination. Another two nights of in-situ heating do not
151 further decrease t/λ but yield an almost flat t/λ evolution (dashed red line).

ACCEPTED MANUSCRIPT

ACCEPTED MANUSCRIPT

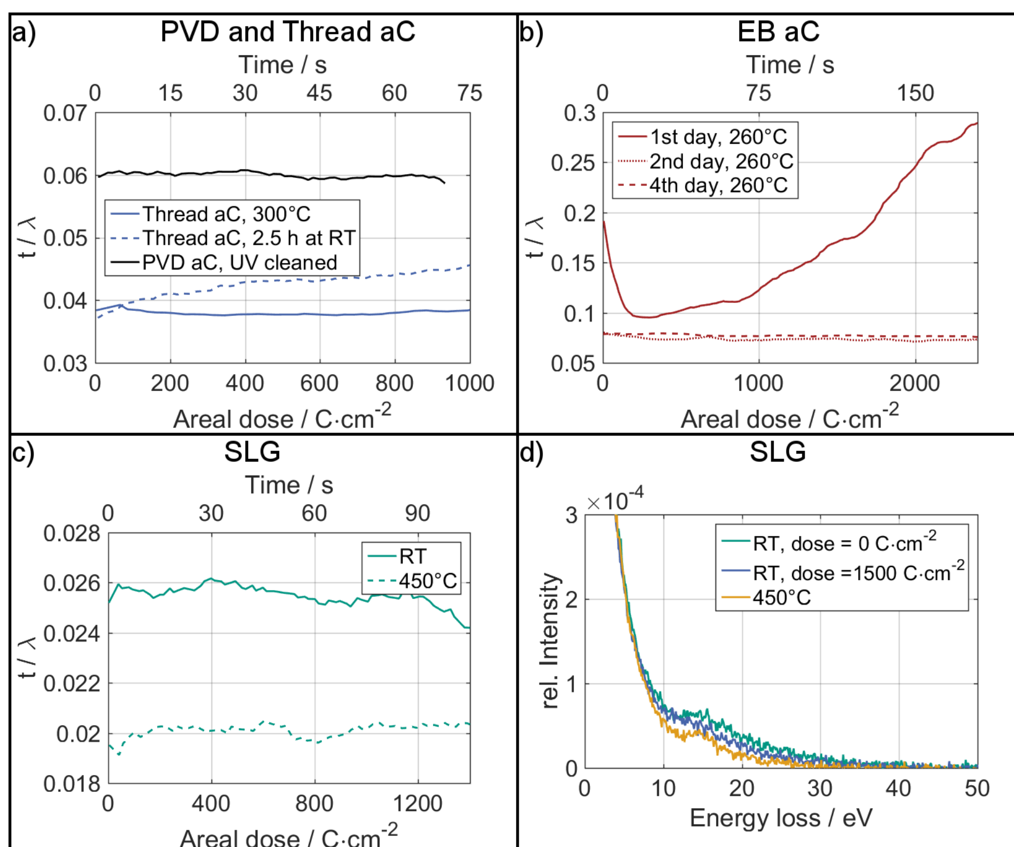

Figure 2: Exemplary t/λ evolutions in dependence of the areal dose for the investigated C thin films and EELS analysis of the SLG thin film. (a) Both PVD and Thread aC show a flat t/λ evolution after the respective cleaning procedures (solid black and blue lines). Leaving the Thread aC thin film at RT for 2.5 h leads to the recurrence of contamination as visible by an increasing t/λ (dashed blue). (b) The EB aC thin film shows a strong initial decrease followed by a slower increase if the thin film is heated directly after insertion in the microscope (solid red line). t/λ is strongly decreased after overnight pumping at 260 °C and only shows a minor decrease (dotted red). After 3 days of in-situ heating, the t/λ evolution is almost flat (dashed red). (c) The SLG thin film exhibits a lower t/λ value after heating to 450 °C overnight (dashed green line) compared to the value measured at RT (solid green). The evolution is flat at elevated temperature and shows a decrease at RT. (d) The EELS spectra of the SLG thin film acquired before (green line) and after (blue) the RT measurement depicted by the blue line in (c) show the decrease in thickness. The EELS spectra acquired at 450 °C shows an overall decreased intensity and exhibits a peak at $\approx$ 15 eV (yellow line). The time axes is calculated for an electron beam current of 60 pA and is for illustration purposes only. (For interpretation of the references to color in this figure legend, the reader is referred to the web version of the article.)

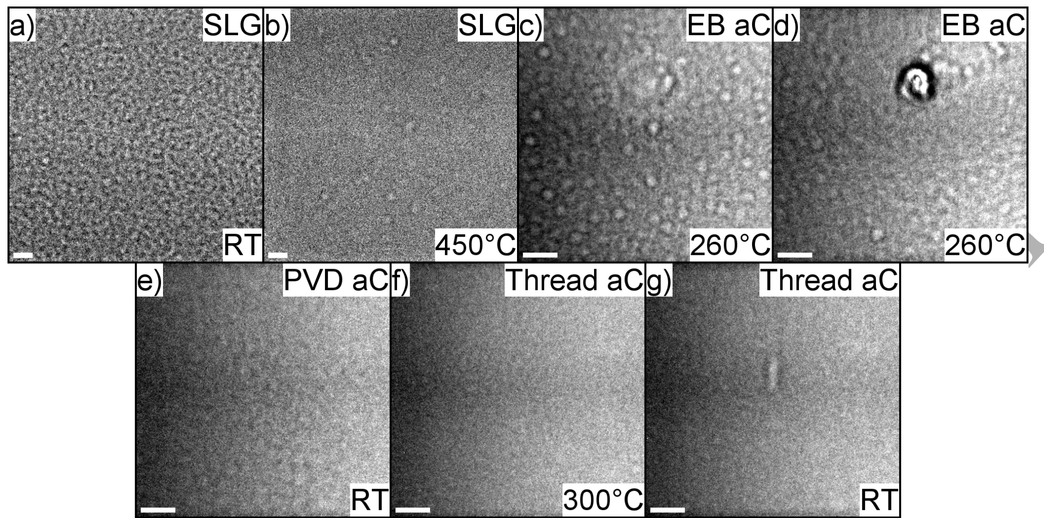

Figure 3: TEM images acquired at strong overfocus (< -1 mm) corresponding to the t/λ measurements displayed in Figure 2 for the SLG thin film at (a) RT and (b) 450 °C, the EB aC thin film at 260 °C (c) after the initial decrease and (d) after the complete t/λ measurement, (e) the PVD aC at RT and the Thread aC thin film at (f) 300 °C and (g) RT. The scale bars have a size of 50 nm.

152 Decreasing t/λ values are also observed for the SLG thin film at RT (solid green line in Fig-
153 ure 2c) while a flat evolution is observed at 450 °C (dashed green line). To avoid contamination
154 and instabilities of the SLG, a beam shower with a dose between 0.1 and 0.15 $\frac{C}{cm^2}$ was carried
155 out directly before the measurements. The lower t/λ value observed at 450 °C and the difference
156 in TEM image contrast between the SLG thin film at RT (Figure 3a) and at 450 °C (Figure 3b)
157 show that there is a thin amorphous layer adsorbed on the SLG at RT. A comparison of the EELS
158 spectra acquired at the beginning (green line in Figure 2d) and at the end (yellow line) of the
159 measurement series at RT corresponding to the t/λ data in Figure 2c suggests that parts of the
160 amorphous layer are removed during electron-beam illumination although a distinct mark of the
161 electron beam is not visible in a TEM image (Figure 3a). While the plasmon peak at 15 eV is
162 clearly visible for the clean SLG at 450 °C (yellow line in Figure 2d), the peak appears blurred
163 at RT, possibly induced by the amorphous layer on the surface (green and blue lines) [24].

164 *3.2. SE evolution*

165 The time evolution of the SE signal gives an insight into the rate at which the SEs escape
166 from the thin film and can provide information on topographic changes or electric potentials
167 on the surface. Figure 4 shows the SE traces for the thin films acquired simultaneously with
168 the t/λ curves displayed in Figure 2. A comparison between the PVD (black line) and Thread
169 aC (blue line) thin film is shown in Figure 4a. The PVD aC thin film exhibits a higher and
170 slowly decreasing SE signal while the SE signal is weaker and almost flat for the Thread aC thin
171 film. For thin films with thicknesses in the range of the SE escape depth, a change of the film
172 thickness can influence the SE yield [16]. As both thin films don't show a significant change
173 in t/λ (Figure 2a), the decreasing SE signal of the PVD aC thin film is likely to result from a
174 charging process.

ACCEPTED MANUSCRIPT

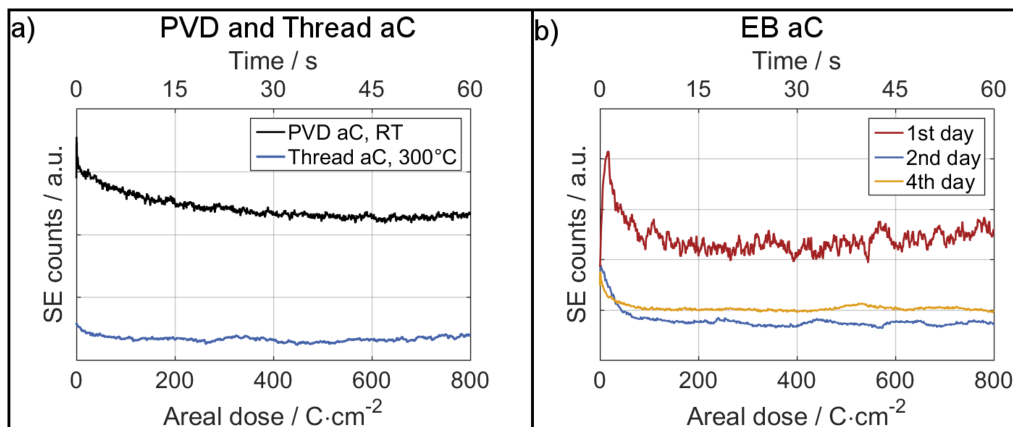

Figure 4: SE evolution depending on the areal dose simultaneously acquired with the t/λ data (Figure 2) for (a) the PVD and Thread aC and (b) the EB aC. The time axes is calculated for an electron beam current of 60 pA and is for illustration purposes only. (For interpretation of the references to color in this figure legend, the reader is referred to the web version of the article.)

Three SE curves for the EB aC thin film at 260 °C on the first (red line), second (blue line) and fourth day (yellow line) in the microscope are depicted in Figure 4b. A strong increase in the SE signal is observed on the first day which is followed by a decrease before the signal slowly starts to rise again (red line). On the second and fourth day, the signal is reduced and initially shows a minor decrease before flattening. Except for the sharp increase on the first day, all curves show the similar shape as the t/λ evolution (Figure 2b). Almost no change in the SE signal is observed for the SLG thin film (supplementary data). The SE trace acquired at RT shows a small decrease after an areal dose of 400 $\frac{C}{cm^2}$ while the trace acquired at 450 °C is flat.

3.3. PCTF evolution

The acquisition of HFPP images in short time intervals and the subsequent analysis of the corresponding power spectra allows to trace the evolution of the PCTF and thus the phase shift induced by an electron-beam induced modification of the illuminated area on the thin film. The PCTF analysis of the HFPP image series acquired for the SLG thin film at RT is shown in Figure 5a by the comparison of two PCTFs from the beginning (solid green line) and the end (dashed green line) of the respective series. In Figure 5a a shift between the initial (solid green line) and the final (dashed green line) PCTF can be observed. The shift of minima and maxima towards higher spatial frequencies (dashed green line) indicates that an additional negative phase shift is induced on the unscattered electrons for the HFPP image acquired at the end of the series. The amount of phase shift is determined to $\phi_{PP} \approx$ -0.2 π and can be attributed to negative charging of the irradiated area on the SLG thin film. The shift continuously increases for spatial frequencies below 0.02 nm^{-1} but is constant for higher spatial frequencies. This suggests that the size of the phase shift tails caused by the charged area, which is *not* identical to the beam diameter, does not exceed 0.02 nm^{-1} corresponding to a real-space disc with a diameter of $2{\cdot}L{\cdot}\lambda_e{\cdot}0.02$ nm$^{-1}{\approx}250$ nm with the camera length L≈3 mm.

The results for the PVD aC, which was UV cleaned ex situ and analyzed at RT, are depicted in Figure 5b. The evolution of the PS determined from the power spectra of the HFPP images shows

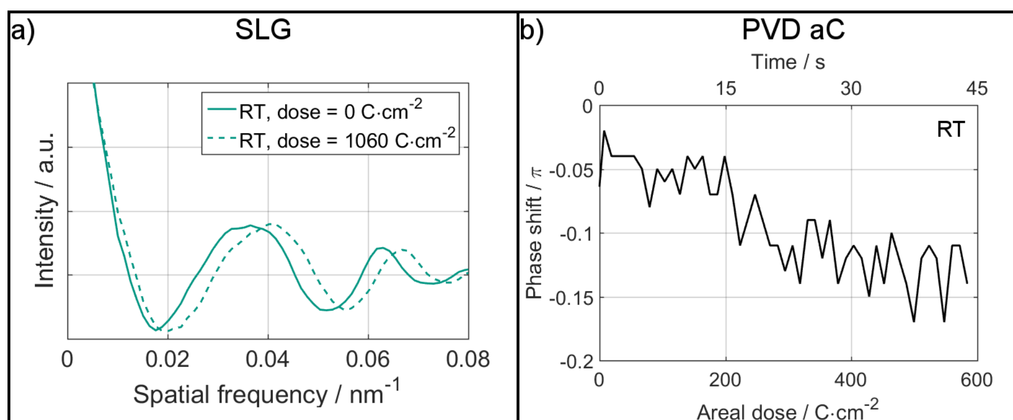

Figure 5: PCTF analysis of the SLG and the PVD aC thin films at RT. (a) Comparison of the initial (solid green line) and the final PCTF (dashed green line) of the HFPP image series shows a strong shift of Thon rings towards higher spatial frequencies. (b) Phase shift evolution for the UV cleaned PVD aC thin film at RT directly after insertion in the microscope shows a small negative phase shift. The time axes is calculated for an electron beam current of 60 pA and is for illustration purposes only. (For interpretation of the references to color in this figure legend, the reader is referred to the web version of the article.)

201 the buildup of a small negative phase shift of ≈ -0.15 π which can be attributed to a negatively
202 charged area on the thin film. If the SLG and PVD or Thread aC thin films are heated overnight
203 at 450 °C and 275 °C in the microscope respectively, no phase shift or change in the PCTF is
204 measured (supplementary data). This reveals that the heated SLG, PVD aC and Thread aC thin
205 films are stable upon focused electron-beam illumination up to areal doses of 1200 $\frac{C}{cm^2}$ and are
206 not prone to neither positive nor negative charging.

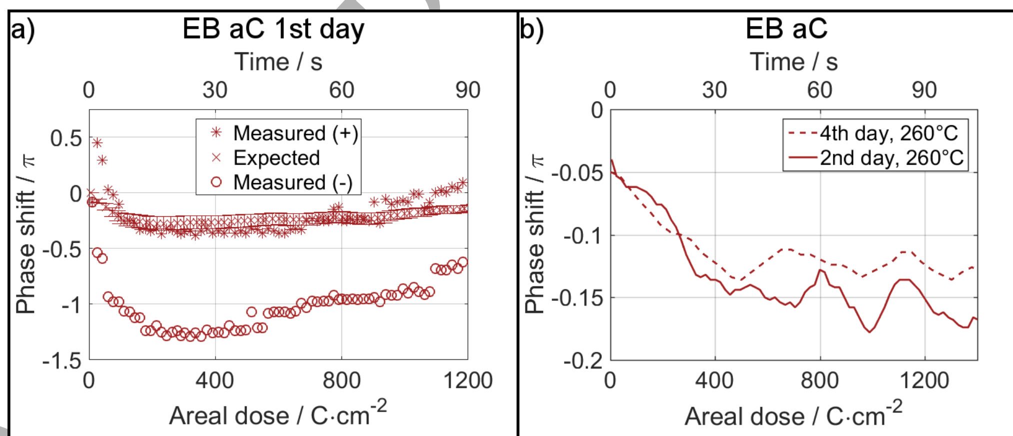

Figure 6: PCTF analysis of the EB aC thin film. (a) The measured phase shift evolution determined from the acquired HFPP images can be interpreted as initially positive (asterisk) or negative (circles) and is compared with the phase shift expected from the thickness decrease of the EB aC (x). (b) Phase shift evolution for the EB aC thin film on the 2nd (solid red) and 4th day (dashed red) of heating to 260 °C in the microscope shows a small negative phase shift. The time axes is calculated for an electron beam current of 60 pA and is for illustration purposes only. (For interpretation of the references to color in this figure legend, the reader is referred to the web version of the article.)

ACCEPTED MANUSCRIPT

ACCEPTED MANUSCRIPT

The analysis of the phase shifting behavior of the EB aC thin film is depicted in Figure 6. The determination of the phase shift step between two subsequent power spectra is possible only in the interval between -0.5π and 0.5π because a shift of π leads to the identical power spectrum. This implies that a measured phase shift between two power spectra of 0.5π is ambiguous and could be as well interpreted as -0.5π. In the case of the EB aC thin film at 260 °C directly after insertion in the microscope, we initially measure a phase shift step of close to 0.5π which can be interpreted either as positive (red asterisks in Figure 6a) or negative charging (red circles). After the initial phase shift step, the phase shift evolution tends to negative charging followed by a slow increase for larger areal doses in both cases. The decrease in thickness obtained from the t/λ measurements (Figure 2b) can be converted in an expected decrease in phase shift if the mean inner electrostatic potential (MIP) and the inelastic mean free path λ (MFP) of the material are known [25]. The inelastic MFP can be estimated from the measured film thickness during evaporation and acquired EELS spectra to be λ = 150 ± 10 nm. The MIP is assumed to be 9 ± 1 V which is a common value for aC thin films [16, 26, 27]. The red crosses in Figure 6a show the expected phase shift evolution with the error bars reflecting the uncertainty in the inelastic MFP and the MIP. A comparison of the measured and expected phase shift shows that an additional phase shift of up to ≈ -π must be present for the negative phase shift interpretation (red circles). In case of the positive phase shift interpretation, the measured (asterisk) and expected (+) curves agree well except for the initial discrepancy which could be explained by positive charging. If the EB aC thin film is consecutively heated to 260 °C, a small negative phase shift is observed after both one and 3 days in the microscope (Figure 6b). As the corresponding t/λ evolution is almost flat (Figure 2b), the phase shift is supposed to originate from negative charging of the thin film.

3.4. XPS measurements

To further study the apparent differences between the PVD and EB aC thin films, XPS experiments were conducted. Table 2 shows the results obtained for both films with and without surface cleaning and the corresponding XPS spectra can be found in the supplementary data. The C1s line is composed out of several peaks which can be attributed to different C bonds [28–30]. The first component is found at 284.4 eV and corresponds to sp^2-hypridized C atoms while the second peak at 285.0 eV can be attributed to sp^3-hypridized carbon atoms and bonds between C and H. Two more peaks of much smaller intensity at ≈ 286 and 288 eV can be attributed to a CO or C=O contamination formed at the surface of the samples due to air exposure. The fith contribution at a binding energy of ≈ 290 eV is linked to π-π^* transitions.

The analysis of the PVD aC thin film reveals the composition of the carbon bonds for the uncleaned and cleaned thin film (Table 2). In both cases, the peak corresponding to the sp^2-hybridized C-C bonds has the highest intensity and slightly increases from ≈ 60 to 70 % due to the cleaning process. The binding energy of the sp^3 bonds in the thin film and possible C-H bonds originating from contamination is identical and amounts to ≈ 27 and 23 % before and after the cleaning process, respectively. The same trend is observed for the bonds between C and O which decrease by a factor of ≈ 2 as a result of cleaning. The fifth contribution to the C bonds can be attributed to π-π^* transitions and amounts to ≈ 3 % in both cases.

The sp^2 bonds contribute only 17 % to the overall C bonds of the uncleaned EB aC thin film while ≈ 68 % can be attributed to sp^3 C-C or C-H bonds. Also the contribution from the C-O and C=O bonds is increased while the peak at 290 eV is missing. Cleaning of the EB aC thin film results in a strong change of the peaks (supplementary data) which now more closely resemble the shape of the PVD aC thin film. This is also reflected by the ratio between sp^2 bonds (66 %)

bond / %	PVD aC uncleaned	PVD aC cleaned	EB aC uncleaned	EB aC cleaned	binding energy / eV
C-sp^2	60.5	69.8	17.0	65.9	284.4-284.5
C-sp^3 / C-H	26.5	22.8	67.5	27.2	285
C-O	6.8	3.0	9.1	3.7	286.7-286.8
C=O	3.1	1.6	6.4	3.2	288.5-288.6
C π	3.1	2.8	0	0	290
C	88.7	97.8	70.5	71.4	280-294
O	10.2	1.8	21.3	13.6	527-537
Cu	0	0.1	3.8	10.6	925-965
Si	1.1	0.3	4.4	4.4	97-106

Table 2: Peak energies and percentages determined from the XPS measurements on the PVD aC and EB aC thin films displayed in the supplementary data. The relative percentage of the C bonds and the complete atomic composition is shown for uncleaned and cleaned thin films.

253 and sp^3/C-H bonds (27 %) which lies between the values of the uncleaned and cleaned PVD aC
254 thin film. Also the content of C and O bonds has decreased while π-π^* transitions still are not
255 present in the cleaned EB aC thin film.

256 In addition to C, additional elements were found which are listed in Table 2. The presence
257 of Si (< 5 %) is attributed to contaminants while Cu originates from the Cu support grids of the
258 thin films. The Cu signal is negligible for the PVD aC thin film but is a significant contribution
259 for the EB aC thin film, especially after the cleaning procedure (> 10 %). The O signal strongly
260 decreases due to the cleaning procedure corresponding well to the decreasing amount of C-O and
261 C=O bonds. The remaining O can be linked to bonds with Si and Cu.

262 The XPS data together with a residual gas analysis within the Hitachi HF3300 (supplemen-
263 tary S2) reveal the presence of different species on the C thin films and in the residual gas atmo-
264 sphere. Clearly, C atoms are the main constituents of the C thin films but oxygen and hydrogen
265 atoms are as well present, mainly as adsorbates on the thin-film surfaces. As C-H bonds can-
266 not be distinguished from C-C bonds in XPS, the amount of hydrogen on and in the thin-film
267 surfaces remains unclear. However, after a suitable cleaning procedure, only a small number of
268 adsorbed molecules remain. In a transmission electron microscope, where water has the highest
269 partial pressure, water molecules will as well be present on the surfaces of the specimen.

270 *3.5. Analysis of published data on HFPPs*

271 For a comparison of our experimental results with previous studies on aC charging and HFPP
272 performance, we analyzed the HFPP image series from [14] (supplementary movies S1 and S2)
273 and [31] (supplementary movie 1) to extract the phase shift induced by the HFPP during settling.
274 Both groups used an aC thin film very similar to the EB aC analyzed in this work and worked
275 at a thin film temperature of 60 °C and 225 °C [14] and 260 °C [31]. The beam diameter on the
276 thin film was 1 μm and 25 nm for the series acquired at 225 °C (red line in Figure 7a) and 60
277 °C (blue line in Figure 7a), respectively. The beam diameter is specified to be between 20 and
278 100 nm for the HFPP image series from [31] whose analysis is depicted in Figure 7b.

279 Figure 7a shows the phase shift evolution for the HFPP operated at 225 °C (red line) which
280 starts at $\approx$ -0.25 and increases up to a phase shift of almost $-\pi$ without reaching a plateau. If the
281 thin film is kept at only 60 °C, the phase shift evolution differs. The phase shift also starts with
282 an increasing negative phase shift but tends towards a positive phase shift already after a few

ACCEPTED MANUSCRIPT

ACCEPTED MANUSCRIPT

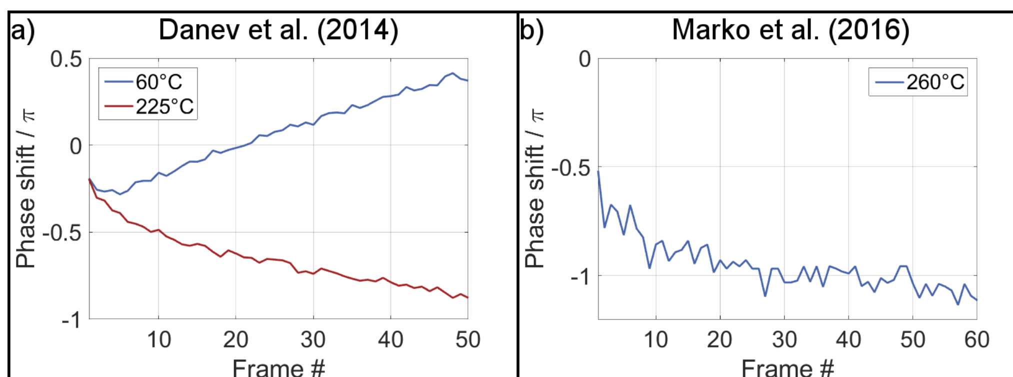

Figure 7: Determination of the PS of HFPP image series from (a) [14] and (b) [31].

frames followed by an almost linear increase (blue line in Figure 7a). The phase shift evolution determined from the HFPP image series acquired at 260 °C (Figure 7b) is similar to the data at 225 °C (red line in Figure 7a): The phase shift initially starts at -0.5 π and further increases to $-\pi$.

4. Discussion

In this section we discuss the experimental results and deduce the underlying microscopic phenomena responsible for the observed charging effects. We first assess the conditions under which charging occurs for the PVD aC, Thread aC and SLG thin films which show comparable charging characteristics. Electron-stimulated desorption (ESD) is suggested as the reason for the observed charging effects. A model of the charging phenomenon is established including the simulation of the electrostatic potential distribution followed by a discussion of the properties influencing the charging. The behavior of the EB aC thin film which deviates strongly from the other thin films is explained by structural differences. Finally, we discuss results from literature for which the presented model is a possible explanation and give an overview over the various HFPP implementations.

4.1. Conditions for charging effects

The assumption that thin films with reasonable conductivity, including C thin films, do not charge under electron-beam illumination was disproved by Brink et al. [2] who observed charging of aC thin films in cryo TEM. Our experimental results, however, indicate that there are conditions under which C thin films do not show observable charging effects. Heating the Thread aC, PVD aC or SLG thin films overnight to temperatures of 275 °C and 450 °C, respectively, leads to a thin film where no measurable thickness change or charging-induced phase shift can be observed (c.f. Figures 2a and c, supplementary data). As both PVD aC and SLG thin films exhibit charging if they are kept at RT (Figure 5) the increased temperature has to cause a modification of the thin films or their surfaces preventing their charging. As structural changes of the thin films such as crystallization are not observed in the conducted experiments, it seems likely that adsorbed molecules on the thin-film surfaces are a responsible cause of the charging effects. This implies that the PVD and Thread aC thin films themselves do not exhibit non-conductive

311 surface sheets as suggested, e.g., in [9]. Even the Thread aC thin film with a thickness <7 nm
312 is stable up to electron doses of at least 1200 C/cm^2, demonstrating that the thin film does not
313 show any charging or thickness changes.

314 The fact, that the thin films have to be kept at an elevated temperature for a prolonged pe-
315 riod of time to prevent charging, indicates that desorption processes are likely to be involved.
316 Surface layers of adsorbates are present on the thin film shortly after insertion in the micro-
317 scope. A common type of adorbates are hydrocarbon molecules which were identified as the
318 source of contamination buildup in a transmission electron microscope [32]. In the following,
319 the expression 'contamination' is used for cases, where a deposition of material is induced by
320 the illuminating electron beam. Hydrocarbon molecules are physiosorbed on the surface with a
321 low adsorption energy and are mobile on the thin-film surface. This is indicated by the fact that
322 heating to 275 °C (kT≈47 meV) overnight is sufficient to cause desorption of the hydrocarbon
323 molecules [16]. The experimental results for the PVD aC and the SLG thin film conducted at
324 RT, however, show the absence of contamination which can be inferred by the flat t/λ evolution
325 (Figure 2a and c). Contamination is inhibited by a removal of the hydrocarbon molecules in
326 a previous UV cleaning step (PVD aC) and by beam shower (SLG) which immobilizes hydro-
327 carbon molecules in an area much larger than the beam diameter [16]. Despite the absence of
328 mobile hydrocarbon molecules on the thin film surface, negative charging effects are observed
329 which are supposed to result from an additional, immobile, surface layer. The presence of such a
330 surface layer, adsorbed with higher adsorption energy, was already assumed to be the reason for
331 the measurement of similar diffusion coefficients for different thin-film materials [16]. As water
332 is the most frequent molecule in the residual gas atmosphere of the Hitachi HF-3300 (supple-
333 mentary data) and is known to easily adsorb on virtually any surface, it is reasonable to assume
334 that H_2O molecules are the dominant species forming the immobile surface layer.

335 In cases where charging was observed, the sign of the measured phase shift was negative
336 for all thin films corresponding to a negatively charged area on the thin film. To understand the
337 presence of a negative charge, the origin of phase shift induced on electrons during propagation
338 through a thin film is reviewed. A homogeneous amorphous thin film is an object with a net
339 charge of zero. Nevertheless, a positive phase shift is observed for transmitted electrons which
340 is commonly explained by the MIP [25]. The physical reason is the difference in spatial distri-
341 bution of positive and negative charges within the thin film. The positive charge at atomic nuclei
342 is highly localized while the electrons are delocalized, especially the conduction band electrons.
343 Fast electrons propagating through the film gain a phase shift mainly caused by the localized pos-
344 itive charges which are only partially screened by the core electrons in the thin film. The polarity
345 of charge which is more localized determines the sign of the induced phase shift. The observation
346 of negative charging on the C thin films therefore has to be caused by a more localized negative
347 charge than positive charge within the illuminated area compared to the surrounding thin film.
348 In contrast to suggesting the presence of additional, more localized, electrons in the illuminated
349 area, we attribute the negative charging to a *removal* of adsorbed water molecules from the thin
350 film surface. The process causing the removal of adsorbed water molecules and the resulting
351 charging effects are discussed in the following sections.

352 *4.2. Electron-stimulated desorption can cause negative charging*

353 In the previous section we claimed that the removal of water molecules from the thin-film
354 surfaces is responsible for the negative charging of the thin films. Here we propose that the
355 underlying physical process for removal of adsorbed water is electron-stimulated desoprtion
356 (ESD). ESD was intensively studied in the last century for numerous surfaces and molecules,

ACCEPTED MANUSCRIPT

357 atoms or molecular fragments [33, 34]. In the corresponding experiments, low-energy electrons
358 (<500 eV) were used to induce the desorption of adsorbates which were then analyzed using
359 mass spectrometry. The threshold energy for ejecting ions or neutral molecules is in the range of
360 5 - 20 eV with neutral species having a lower threshold [33]. In (S)TEM, the incident electron
361 energy of 300 keV is significantly higher than in typical ESD experiments resulting in a drasti-
362 cally decreased cross section for primary electrons to cause ESD. However, SEs generated in the
363 thin film have typical kinetic energies of up to 100 eV and thus can induce ESD. ESD indeed
364 plays an important role in focused electron-beam induced processing (FEBIP) where electron-
365 beam illumination is used in combination with suitable precursor gases to, e.g., deposit or etch
366 nm sized structures on sample surfaces [35–37].

367 The principle of ESD is schematically depicted in Figure 8a: An illuminating primary elec-
368 tron (PE) generates SEs within the C thin film. The SEs can leave the thin film if their kinetic
369 energy is larger than the work function of the material and can then be detected by a suitable de-
370 tection system. During propagation through the thin film, the SE can initiate additional reactions
371 including the desorption of adsorbed molecules from the thin-film surface. The probability for a
372 PE to induce ESD is then dependent on the SE yield y, which was determined by measuring the
373 total incident current and the return current from ground to be y=0.001-0.01 for the investigated
374 thin films, multiplied by the probability of a SE to initiate the desorption of a water molecule.
375 Additionally, the spatial and energy distribution of the generated SEs and the activation energy
376 needed to cause the desorption of the adsorbed molecule play a role. With the areal PE current
377 density of $\approx 1.6 \cdot 10^7$ $e^-/(nm^2s)$ used in the experiment and a conservative estimate that only one
378 of ten thousand generated SEs induces the desorption of an adsorbed molecule, the PE-induced
379 desorption rate results in 2-16 molecules/(nm^2s) depending on the SE yield of the thin film. This
380 estimated cross-section is high enough to be considered as a possible cause for the observed
381 charging phenomenon.

382 However, the removal of material by ESD and the associated thickness decrease alone cannot
383 explain the observed charging phenomena. Both the PVD aC and SLG thin films show a flat or
384 only slightly decreasing t/λ evolution (Figure 2a and c) suggesting that the desorbed molecules
385 represent only a very small fraction of the actual film thickness. On the other hand, the negative
386 phase shift is clearly detectable (Figure 5) showing that an additional effect has to be present to
387 cause a negative charging of the illuminated area. This negative charging can be attributed to
388 a local change in work function (WF) in the illuminated area which is caused by ESD. Studies
389 on the effect of ad- or desorption of water molecules on clean metal surfaces revealed that the
390 WF of the metal decreases if water is adsorbed on its surface [38–42]. The water molecule on a
391 surface can be interpreted as a dipole with the positive charge pointing towards the vacuum [41]
392 as schematically depicted in Figure 8b. This dipole layer represents a potential step δV which
393 leads to an effectively decreasing WF of the metal and can amount up to a few eV depending
394 on the properties of the metal. Although aC thin films are neither metallic nor crystalline, an
395 adsorbed water layer with the hydrogen atom pointing to the vacuum will have the same effect
396 on the WF of the investigated aC and SLG thin films. The effect on the WF is shown in Figure 9b:
397 The WF in the central, 'dry', disk with radius R is equal to the nominal WF of C, ϕ_C, while it is
398 decreased in the 'wet' areas by the adsorbed water to $\phi_1 = \phi_C - e \cdot \delta V$.

399 The measurements of the WF change upon water adsorption showed an increasing δV with
400 increasing water coverage which saturates once a monolayer of water is adsorbed on the surface
401 [41]. The studies were carried out under ultra-high vacuum (10^{-10} mbar) and temperatures of
402 liquid nitrogen (77 K). Compared to the conditions in a transmission electron microscope, the
403 pressure is significantly reduced by more than 2 orders of magnitude and the temperature is

ACCEPTED MANUSCRIPT

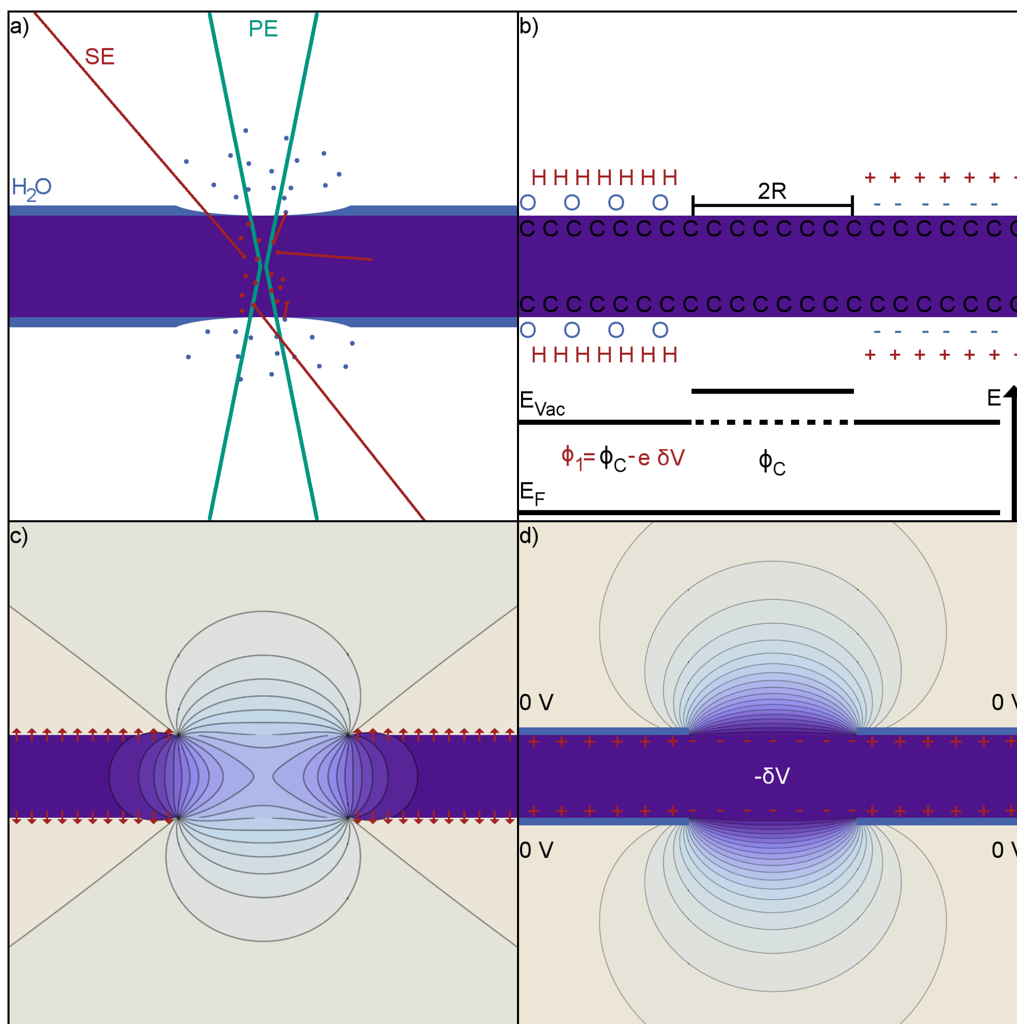

Figure 8: Schematic illustration of the principle of electron-stimulated desorption and its effect on the charge and potential distribution. (a) An illuminating primary electron (PE, green) is generating SEs (red) in the C thin film (purple) with a few exemplary SE trajectories indicated. A part of the SEs can initiate the desorption of adsorbed H_2O molecules from a surface layer (blue). (b) The adsorbed water layer forms a dipole with the hydrogen (+) end pointing to the vacuum. The water layer effectively reduces the WF ϕ, i.e., the energy difference between vacuum E_{Vac} and Fermi-energy E_F by eδV. (c) Electrostatic potential distribution for two interrupted dipole layers (red arrows) in empty space *without* carbon film. The potential range is between the step -δ V (purple) caused by the dipole layer and 0 V (white) (d) Potential distribution between -δ V (purple) and 0 V (white) for an interrupted water layer on the surface of a C thin film (purple). (For interpretation of the references to color in this figure legend, the reader is referred to the web version of the article.)

lowered by more than 200 K. Taking into account the relatively high temperature (≥300 K), we assume that only a small fraction of a monolayer is adsorbed on the thin films if they are kept in the microscope overnight.

It is emphasized that, although the central area is charged negatively, the thin film as a whole is still a charge neutral entity. ESD can cause the desorption of neutral molecules or charged

409 fragments from the surfaces. Charges possibly left behind on the thin-film surface by desorption
410 of ions are however rapidly compensated by a current from ground, if the film has sufficient
411 electrical conductivity and no non-conducting surface barrier; a necessity which is supposedly
412 given for the investigated thin films.

413 *4.3. Electrostatic potential simulations*

414 Water adsorbed on a surface can be interpreted as a surface dipole layer with the positive
415 charge pointing to the vacuum [41] which represents a potential step δV=p/(A ϵ_0) where p is
416 the dipole moment of a water molecule, and 1/A is the areal number density of water molecules
417 on the surface. This potential step effectively changes the WF of the material [41]. If water
418 is desorbed by ESD in the area illuminated by the PEs, this surface dipole layer is interrupted
419 leading to a disturbance of the previously homogeneous electrostatic potential distribution on the
420 thin-film surface. To assess the resulting change of the charge distribution and the impact on the
421 phase shift induced on electrons propagating through the potential, we first analytically calculate
422 the potential distribution of two interrupted dipole layers in empty space, e.g. *without* C thin film
423 using elliptic integrals under the assumption that the field from one layer does not influence the
424 other. This and the following calculations are conducted with radial symmetry and the central,
425 interrupted, area in Figure 8 is actually a circular region. The result obtained without C thin film
426 is depicted in Figure 8c with the potential ranging from -δV (purple) to 0 V (white). Here, the
427 negative potential is limited to the area between the dipole layers. The phase shift induced on a
428 primary electron passing the circular, interrupted, area (q=0) is calculated by integration of the
429 potential along the beam path and results in -C_E t δV. This phase shift is identical to the phase
430 shift induced on a scattered electron passing the 'wet' area far away from the center (q>0) due
431 to the potential between the two dipole layers resulting in a net phase shift of 0.

432 If a C thin film, for now assumed to be a metal, is put in between the two interrupted dipole
433 layers, the electrons in the conduction band will 'see' the potential distribution caused by the
434 water dipoles. The electrons in the central, 'dry', part, where the water was removed by ESD,
435 will have a lower energy than the electrons in the surrounding, 'wet', areas. If the radius of the
436 illuminated patch R is much larger than the film thickness, the potential difference within the thin
437 film will amount to δV. The electrons close to the surface in the wet areas of the thin film will
438 then drift to the dry patch and lead to a local negative charging of the dry patch until the potential
439 in the C thin film is in an equilibrium state. Figure 8d shows the C thin film, the interrupted
440 water layer on the surfaces and the resulting potential distribution. The exact distribution of the
441 negative charging is not accessible analytically and is only indicated in the C thin film by the
442 markers (+ and - in Figure 8d). The redistribution of charges causes a potential of -δV (purple)
443 in the C thin film and in the area just above the dry patch while the potential directly above the
444 dipole layer is 0 V (white). This situation is identical to assuming a thin film with a circular patch
445 at a negative potential -δV in the illuminated area.

446 To reveal the dependence of the phase shift on the amount of WF change, calculations of the
447 electrostatic potential distribution in the vacuum area above a charged thin film were conducted.
448 The illuminated thin film is modeled as a surface with a circular (radius R) unit-step potential
449 variation δV corresponding to the expected change of the WF. The solution of the Laplace equa-
450 tion yields the potential distribution displayed in Figure 8d and the integration of the potential
451 along a vertical beam path results in the phase shift imposed on electrons propagating through the
452 thin film. In this model, the phase shift imposed on the PEs (q=0) relative to electrons scattered
453 at very high angles (q=∞) is given by

ACCEPTED MANUSCRIPT

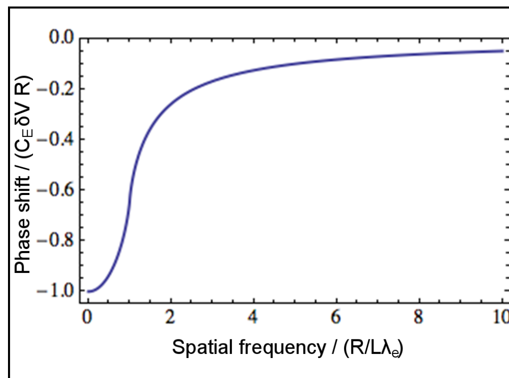

Figure 9: Generic profile of the phase shift imposed on a fast electron propagating through the potential distribution in Figure 8d obtained by integration along the beam path. L is the camera length.

$$\phi_{PP} = C_E \cdot R \cdot \delta V \tag{3}$$

where the interaction constant is C_E=6.53 $\cdot$ $10^6 \frac{1}{m \cdot V}$ for 300 keV electrons [25]. The phase shift imposed on a PE propagating through the area with increased WF is linearly dependent on the radius of the area R and on the amount of WF change δV. It is noted that the radius R of the area is *not* identical with the beam size which will be discussed in the following section. As the WF outside of the circular patch is reduced by the adsorbed water layer, δV is negative which signifies a negative phase shift.

Figure 9 shows the generic phase profile in dependence of the spatial frequency (R/(λ_eL)) obtained by integration of the potential distribution with L being the camera length. The phase profile initially exhibits a steep gradient before evolving into a long flat tail. The top-hat potential assumed in the simulations thus does not result in a top-hat phase shift profile. The long tail implies that even if the patch with changed WF is very small, the electrostatic potential can reach far out and can still affect high spatial frequencies which can complicate the experimental determination of ϕ_{PP}. In practical experiments the shallow gradient above spatial frequencies of 2R/(λ_eL) will be difficult to detect due to the interplay with the defocus and can possibly be interpreted as a boundary of the phase shift tails.

So far, we assumed the C thin films to have metal-like character signifying highly mobile charge carriers within the thin film. For a transition into semi-conducting properties, the charge carrier density and mobility in the thin film will decrease and a space-charge region (SCR) at the interface between wet and dry patch will form. The SCR is infinitesimally small in case of a metal but can be large for semiconductors or insulators. However, as long as the width of the SCR is much smaller than the radius R of the illuminated patch, the total amount of phase shift induced on the primary electrons with respect to electrons scattered to high spatial frequencies remains unchanged. Equation 3 is still valid and only the shape of the phase profile (Figure 9) is affected, i.e., the profile will extend to higher spatial frequencies. As the investigated aC thin films only showed minor charging effects, it is reasonable to assume that their properties are close to a metal-like behavior at the investigated temperatures.

With equation 3, we can compare experimental results with the simulations and estimate a value for δV. In case of the SLG thin film, the spatial frequencies affected by the charged area and

ACCEPTED MANUSCRIPT

482 the resulting phase shift profile can be estimated by an increasing shift of Thon rings (Figure 5a) 483 to be in the order of 0.02 nm^{-1} (≈250 nm). This size can be linked to the boundary $2R/(\lambda_e L)$. 484 Under the assumption, that both, upper and lower, thin-film surfaces are equally charged, the 485 observed phase shift of -0.2 π has to be divided by a factor of 2. δV can then be calculated to be 486 -0.4 V for the SLG thin film at RT which corresponds well to expectations from literature [40].

487 By taking the dipole moment of an isolated water molecule $p_{H_2O}=6.18\cdot10^{-30}$ C·m one can 488 estimate the upper limit of the potential step δV caused by a monolayer of adsorbed water on the 489 surface. With the area A=0.18 nm^2 occupied by a single water molecule in case of full coverage 490 [41] and the vacuum permittivity $\epsilon_0=8.85\cdot10^{-12}$ $F\cdot m^{-1}$, the potential step results in 4 V. This 491 estimation is an upper limit to δV, while in reality the work function decrease is expected to be 492 substantially lower due to three aspects: 1. The dipole moment of chemisorbed water molecules 493 will decrease compared to an isolated water molecule due to electronic structure relaxation and 494 charge transfer with the C atoms of the surface; 2. We expect the coverage of the surface to be less 495 than a full monolayer at the studied temperatures and 3. the thin films exhibit a surface roughness 496 which can lead to a loss of dipole moment due to a misalignment of the water molecules with 497 respect to the thin-film surface.

498 We assumed that water is the main component of the adsorbed surface layer and that water 499 reduces the WF of the investigated C thin films. However, it is possible that impurities in the 500 adsorbed water layer or on the film surfaces, such as the presence of metal ions, can change 501 the polarity of the charging or affect the electrical properties such as the WF of the film. As 502 we used double-distilled water for preparation of the thin films, we assume that such impurities 503 are present only in a negligible amount. It is noted, however, that different adsorbed molecules 504 will as well influence the WF of the thin film if their adsorption is linked with a charge transfer 505 between molecule and thin-film atoms. Such a charge transfer will cause a redistribution of 506 charges on the thin-film surfaces. If the adsorbed molecules are removed by ESD in a small area, 507 it will again result in a charging of the thin film in the illuminated area. The presented model is 508 thus also valid for different adsorbates which can be desorbed by ESD and lower the WF.

509 The removal of water in the dry area and the resulting potential distribution not only causes 510 a negative phase shift on transmitting electrons but additionally has an effect on the detectable 511 SE signal. A generated SE can only escape from the thin film if its kinetic energy is larger than 512 the WF. As the WF is restored to the nominal value in the dry area, the energy barrier for a SE 513 to escape from the thin film increases, which leads to a decreasing number of detectable SEs. 514 This effect is indeed observed in Figure 4, where the SE signal is plotted as a function of the 515 areal dose for the different thin films. The SE signal is almost constant for thin films not showing 516 a charging effect such as the SLG thin film at 450 °C (supplementary data). Only a minor ini- 517 tial decrease of the SE signal is observed for the Thread aC at 300 °C where charging also was 518 below the measurable level (<≈0.02 π). On the other hand, a decreasing SE signal is observed 519 for charging thin films such as the PVD aC thin film at RT (Figure 4a). The SLG thin film at 520 RT which shows charging effects seems to have a stable SE signal but a closer look reveals a 521 faint decrease at higher areal doses (supplementary data). Additionally, the SE signal is only ac- 522 quired up to an areal dose of 600 C/cm^2 while the measured phase shift appeared at higher doses 523 (1000 C/cm^2) indicating a possible further decreasing SE signal at doses >600 C/cm^2. Overall, 524 the measured SE traces are consistent with the model of an increasing WF in the illuminated area 525 and a corresponding suppression of escaping SEs.

526 The discussed model is also consistent with the t/λ measurements (Figure 2). The desorption 527 of a thin layer of adsorbed H_2O molecules only has an insignificant effect on the overall t/λ 528 value of an aC thin film resulting in the flat evolution. A measurable decrease of t/λ is only

ACCEPTED MANUSCRIPT

529 observed when the desorbed molecules represent a substantial content of the thin film such as
530 for the SLG thin film at RT or the EB aC thin film on the first day. In those cases, the type of
531 molecule desorbing from the thin film is most likely of hydrocarbon nature possibly containing
532 considerable amounts of water.

533 *4.4. Experimental influences on the charging behavior*

534 The simulations show that the charging model based on an ESD induced change of the WF in
535 the illuminated area is well compatible with the experimental data. According to the simulations,
536 the strength of the charging effect is mainly influenced by the radius R of the charged area and
537 the amount of the induced WF change δV. In this section we assess the main parameters that
538 influence both R and δV in a particular experiment such as, e.g., the thin-film temperature and
539 the beam current density.

540 δV depends on the electrical and structural properties of the thin film and the water coverage
541 of the surfaces. The studies of the change of the WF induced by H_2O adsorbed on metal surfaces
542 showed that the WF decreases with increasing water coverage and saturates once a coverage with
543 one monolayer is reached [41, 43]. The implication for our experiments is that the amount of
544 water adsorbed on the thin-film surfaces has direct influence on δV. The lower the number of
545 adsorbed H_2O molecules on the thin-film surfaces, which is determined by the thin-film tem-
546 perature and structure as well as the partial pressure of water in the residual gas atmosphere,
547 the lower is the observed charging effect. A higher temperature increases the available thermal
548 energy causing more water to desorb and vice versa. Ad- and desorption, however, are relatively
549 slow processes so that a fast change of the thin-film temperature does not immediately change the
550 number of adsorbates on the thin-film surfaces. The adsorption of molecules is also influenced
551 by the morphology of the thin film. A film with high surface roughness or film porosity provides
552 more adsorption sites than a homogeneous thin film meaning that, under identical experimental
553 conditions, the coverage with water can vary between different aC thin films.

554 The residual gas composition in the Hitachi HF-3300 mainly contains water (supplemen-
555 tary data). The higher the partial pressure of water, the higher is the number of adsorbed H_2O
556 molecules on the thin-film surfaces. The vacuum in a transmission electron microscope is not
557 ultra-high and typically in the range of a few 10^{-7} mbar. As the HF-3300 microscope is baked
558 regularly over the weekends, the vacuum stays at values below $5 \cdot 10^{-8}$ mbar and its vacuum is sup-
559 posedly better than in a typical transmission electron microscope. This implies that the amount of
560 adsorbed water and thus the corresponding charging effects are less pronounced in the HF-3300.

561 It is emphasized, that the area on the thin film where the WF change is induced by the
562 illuminating electrons (R) does not have sharp borders but is expected to be diffuse. The ESD
563 of water molecules from the surface layer is generated by SEs with a specific spatial distribution
564 which in general is much broader than the PE beam diameter. Water molecules are therefore not
565 only desorbed in the center of the illuminated area but in an area with the size of the mean-free
566 path of the SEs in the aC thin film. The edges of this area are only reached by a small number
567 of SEs leading to a strong reduction of the ESD rate at larger distances from the beam center.
568 While the water molecules within the illuminated area are desorbed quickly, further illumination
569 with the electron beam will cause an enlargement of the patch where the WF is increased. Longer
570 illumination times should then result in a slowly increasing radius R and observed negative phase
571 shift ϕ_{PP}. The diffuse edges of the dry patch will only influence the phase shift profile (Figure 9)
572 but not the final amount of ϕ_{PP}.

573 The beam current density has a major influence on the charging behavior. The beam current
574 itself is suspected to only have a minor influence on the charging effects if it stays within typical

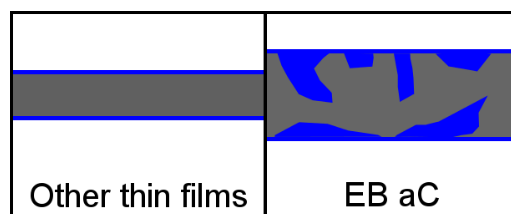

Figure 10: Schematic drawing of the assumed structure for (a) the Thread aC, PVD aC and SLG thin films and (b) the EB aC thin film. The thin films are depicted with a gray color and the blue color indicates adsorbed molecules. (For interpretation of the references to color in this figure legend, the reader is referred to the web version of the article.)

575 values for STEM and if the beam diameter on the thin film is kept constant. A lower beam
576 current then will of course lower the rate at which ESD takes place but it is suspected to not have
577 an influence on the final amount of observable phase shift. The time scale at which water will
578 re-adsorb on the thin-film surface is drastically higher than typical STEM measurement times
579 considering the low partial pressure of water within the microscope. Once all water molecules
580 are desorbed during PE illumination, a steady state is reached. If the beam is switched off, water
581 molecules will start to re-adsorb on the illuminated area and possibly diffuse along the sample
582 surface. However, both processes are assumed to happen in a time scale of minutes and hours
583 which can explain the fact that HFPP patches remain charged for a longer period of time [14, 31].
584 We did not study the longevity of the charged patch in the presented experiments and can thus
585 only speculate about the speed of the re-coverage of the surface with water.

586 In contrast to the beam current, a significant influence on the detectable phase shift is given
587 by the beam diameter. A change in the size of the area in which the WF changes will directly
588 influence the radius R (Equation 3) and thus increase the phase shift induced on transmitting
589 electrons. Here, the beam diameter was small (≈20 nm) compared to the charged area. If the
590 beam diameter is however increased strongly much larger phase shifts could be be achieved.

591 *4.5. Charging of the EB aC thin film*

592 To understand the observed differences between Thread and PVD aC compared to the EB
593 aC thin film which still charges even if it is extensively heated to 260 °C in the microscope
594 (Figure 6b), the structure of the thin films has to be analyzed. The EB aC shows a strong decrease
595 in thickness when illuminated shortly after insertion in the microscope and subsequent heating
596 to 260 °C. t/λ decreases from ≈ 0.2 by a factor of 2 before starting to rise again (Figure 2b). This
597 behavior can be explained if a porous structure of the EB aC thin film is assumed. Without a
598 cleaning step, the EB aC thin film surface and its pores are covered with hydrocarbon molecules
599 (Figure 10b). The initial value for t/λ therefore includes both the thickness of the actual EB aC
600 thin film and of the hydrocarbon molecules. Previous measurements showed that heating of an
601 aC thin film to 275 °C overnight leads to a desorption of the hydrocarbon molecules [16]. The
602 value for t/λ observed on the second day after overnight heating to 260 °C then reflects the actual
603 thickness of the EB aC thin film. This implies that initially, about half of the measured thickness
604 originated from adsorbed hydrocarbon molecules. Assuming that the thickness of an adsorbed
605 hydrocarbon layer is self-limited to a few monolayers, the observed t/λ composition can only be
606 explained by assumption of a porous thin film structure as schematically depicted in Figure 10b.

607 This assumption is confirmed by the comparative XPS measurements of the PVD and EB
608 aC thin films (Table 2). XPS is a technique sensitive to the first few nm of a sample only.

ACCEPTED MANUSCRIPT

ACCEPTED MANUSCRIPT

609 XPS measurements on the aC thin films should reflect the fraction of sp^2-hybridized C atoms
610 which was determined by EELS measurements to be ≈ 70 % independent of the type of aC thin
611 film [16]. However, the binding energy of sp^3-hybridized C-C bonds is identical to C-H bonds
612 meaning that C-H bonds present in hydrocarbon molecules adsorbed on the thin film can affect
613 the determination of the sp^2 to sp^3 ratio. The XPS measurement performed on the as-prepared
614 PVD aC thin film reveals the presence of ≈ 70 % sp^2-hybridized C-C bonds and about 10 % of the
615 total C atoms are bonded with O which can be attributed to surface contamination (c.f. Table 2).
616 After the Ar sputter cleaning procedure, the sp^2 fraction slightly increases to 75 % due to the
617 removal of contaminants and the amount of O bonds is strongly decreased. The experimental
618 results obtained on the PVD aC thin film are well compatible with the results expected for a
619 homogeneous thin film with low roughness and a thin adsorbed contamination layer.

620 A different situation is found for the EB aC thin film. The high percentages of C-O and C-H
621 bonds for the uncleaned thin film are attributed to the presence of large amounts of contamination
622 which almost completely cover the actual thin film. Ar-sputtering removes a substantial part of
623 the contamination but the amount of C bonds with O (9 %) is still significantly higher compared
624 to the PVD aC thin film (4.5 %). This implies that contamination is also present within the actual
625 EB aC thin film indicating a high surface roughness and a porous structure. Additionally, the
626 absence of C π-π^* bonds in the EB aC thin film suggests that graphitic planes are not present in
627 the thin film.

628 The structural differences between the EB aC and all the other C thin films and its significance
629 for the charging effects can be summarized as follows: The PVD aC, Thread aC and SLG thin
630 films are homogeneous and have a very low surface roughness meaning that a limited number of
631 sites are available for molecules to adsorb. In contrast, the high roughness and porosity of the
632 EB aC thin film results in a significantly higher active surface area. Effects which are related
633 to adsorbed surface layers are therefore suspected to be much more pronounced for the EB aC
634 compared to the other C thin films.

635 The rapid decrease in thickness of the EB aC thin film during electron-beam illumination
636 shortly after insertion and heating to 260 °C is recognized as electron-stimulated desorption
637 (ESD) of hydrocarbon molecules. As hydrocarbon molecules desorb overnight at a temperature
638 of 260 °C, the thermal energy available (≈ 45 meV) is sufficient to initiate the desorption pro-
639 cesses. However, the desorption rate is limited and it takes a long time for the contamination to
640 desorb. When the thin film is illuminated shortly after heating to 260 °C, the time at elevated
641 temperature was not sufficient for all molecules to desorb. The focused electron-beam illumina-
642 tion then stimulates the desorption of the remaining adsorbed molecules in the illuminated area
643 leading to the observed rapid decrease in thickness. In parallel with ESD, but at a much slower
644 rate, the deposition of a contamination layer takes place [16]. The deposition of contamination
645 becomes dominant once all molecules in the illuminated area, including the water molecules
646 chemisorbed on the surface, are desorbed, i.e. there is no more material to be removed. Contam-
647 ination may still be present as mobile hydrocarbon molecules can diffuse along the film surface
648 to the irradiated area [16, 32]. After the desorption ceases, surface sites of the carbon thin film
649 itself are available for hydrocarbon molecules to bond and to form a contamination layer leading
650 to the observed thickness increase. This interplay between desorption and deposition can also be
651 observed in the analysis of the phase shift evolution of the Volta PP at 60 °C (Figure 7a, [14]).
652 The evolution first shows a negative phase shift caused by ESD followed by a trend to positive
653 phase shifts induced by contamination. A detailed description of the involved physical processes
654 is not possible solely from the presented experiments and so several parameters remain unclear,
655 e.g., the ratio between desorption and deposition or the mixture of molecules present on the thin

ACCEPTED MANUSCRIPT

film.

The time resolution of the PCTF measurements is not sufficient to unambiguously resolve the phase shift evolution of the EB aC directly after insertion (Figure 6a). The initial phase shift step has a value close to $\pi/2$ which can be interpreted as a positive or negative phase shift. As the following phase shift steps are smaller than $\pi/2$ and tend toward a negative phase shift, the first guess is that the initial phase shift step is as well negative, which will be denoted as 'negative interpretation' in the following. The observed thickness change (Figure 2b) can be used to estimate an expected phase shift if values for the MIP (here 9 V) and the inelastic MFP (150 nm) are assumed (Figure 6a). A comparison with the negative interpretation shows that the measured phase shift is about π larger than expected from the thickness decrease (c.f. Figure 2b and 6a). In addition to the decreasing thickness, a negative charging must occur to explain the higher negative phase shift. This negative charging could be explained by ESD and an accompanying WF change. As hydrocarbon molecules are only physiosorbed on the thin-film surface, a strong influence on the WF is not expected and the major part of the WF change is assumed to originate from ESD of water.

The phase shift evolution on the first day can also be interpreted as an initial positive phase shift step. This positive phase shift could be caused by a positive charging of the irradiated area, e.g., by positive charge trapping in the insulating hydrocarbon layer. As the adsorbed hydrocarbon molecules are rapidly desorbed during further illumination, the positive phase shift is present for only a few seconds and measurement points. After desorption of the adsorbed hydrocarbon molecules, the phase shift evolution for an initial positive phase shift step follows the expected evolution from the t/λ measurements (Figure 6a) indicating a lack of charges in the illuminated area.

The presence of a large amount of hydrocarbon molecules on the EB aC thin film shortly after insertion and heating of the thin film complicates the interpretation of the experimental results and we can only speculate on the involved processes. Both, positive and negative, initial phase shift possibilities can be explained by either negative or positive charging of the illuminated area. The data acquired after two and four days of consecutive heating of the thin film however clearly show the effect of the different structure of the EB aC compared to the other thin films. After one day of heating to 260 °C, most hydrocarbon molecules are desorbed from the thin-film surface and the observed negative phase shift of $\approx$-0.15π can be explained by ESD of water and an accompanying WF change. The amount of water adsorbed on the thin film is suspected to be higher compared to the other thin films due to the structural differences such as increased surface roughness which leads to the stronger charging of the EB aC thin film. The amount of measured phase shift only slightly decreased from the second to fourth day of consecutive heating in the microscope indicating that an equilibrium state between the number of adsorbed H_2O molecules on the thin-film surfaces and the partial pressure of water in the residual gas atmosphere is established. The negative charging can also be observed in the SE signal. The EB aC thin film exhibits a decreasing SE signal caused by the increased WF and the drop is decreasing with the time kept in the microscope (Figure 4b) corresponding well to the observed decreasing induced phase shift (Figure 6b).

4.6. Implications for HFPP imaging and related charging phenomena

The local change of the WF of a thin film induced by ESD of surface layers can affect numerous applications in EM. The effect causes a more subtle type of charging with induced phase shifts below π which nevertheless can hamper a correct analysis of acquired data. Here we dis-

ACCEPTED MANUSCRIPT

701 cuss several possible applications, where ESD and an accompanying change of the WF can play
702 a significant role.
703 The described charging phenomenon is a plausible explanation for the functionality of the
704 HFPP [8, 31] and its implementations including the Volta PP [14]. The aC thin film used as Volta
705 PP in [14] and as HFPP in [31] was fabricated using the identical device type as the EB aC thin
706 film analyzed in this work. The Volta PP is used at a temperature of 225 °C which is slightly
707 lower than the EB aC thin-film and HFPP temperature of 260 °C and the beam diameters were 1
708 μm, 20 nm and 100 nm, respectively. The thin films show negative charging upon electron-beam
709 illumination with the reported phase shift being about four times higher for the Volta PP than the
710 results presented here (c.f. Figures 6b and 7a). An ESD-induced change of the WF is a plausible
711 explanation for the functionality of the negatively charged PPs. Several factors lead to the higher
712 negative PS of the Volta PP: Firstly, the larger beam diameter on the Volta PP causes a larger
713 patch radius R yielding a higher phase shift. Secondly, it is reasonable to assume that the vacuum
714 in the regularly baked Hitachi HF-3300 is better than in the cryo microscopes used in [14, 31]
715 where water supposedly has a higher partial pressure. Thirdly, together with the lower operating
716 temperature of the Volta PP the higher partial pressure of water leads to more water molecules
717 adsorbed on the thin-film surface leading to a higher change in WF due to ESD. Danev et al.
718 [14] claimed a Volta potential induced by the illuminating electron beam to be the explanation
719 for the functionality of their experimental observations. Our findings and the established ESD
720 model now give the physical explanation for the origin of the change in potential. ESD of water
721 molecules from the surface leads to a local change in the WF of the aC thin film which can be
722 interpreted as a local negative charge or potential inducing the observed PS.
723 Figure 11 gives a graphical overview over the possible implementations of a HFPP which
724 all have in common that an electron-beam induced process causes an additional phase shift of
725 the PEs. Hettler et al. [16] reported that contamination deposited by an electron beam with
726 high current density can be used as a HFPP if the deposition process can be controlled. This
727 control, however, is difficult to achieve and has not been applied yet. The first implementation
728 of a HFPP by Malac et al. [8] was explained by positive charges in insulating layers left behind
729 by escaping SEs [44]. There are further possible implementations of HFPP concepts, especially
730 if material other than aC is utilized. Any electron-beam induced process which is separating
731 charges perpendicular to the electron beam can be a possible explanation. Structural changes of
732 a material induced by electrons can, e.g., change the MIP of the thin film and lead to the desired
733 phase shift. Additionally, local heating could be used to induce diffusion of specific elements in
734 alloys or to induce electric fields in thermoelectric materials.
735 Our findings have several implications on the applicability of the negative-charging variation
736 of the HFPP. As the EB aC has a high surface roughness, local structure variations are highly
737 probable. The PS resulting from focused electron-beam illumination due to ESD and the ac-
738 companying WF change will depend on the local structure due to different amounts of adsorbed
739 water and local variations of the electronic properties. The established PS is therefore not stable
740 and varies with the positioning of the illuminating electron beam on the aC thin film. This is re-
741 flected by the strongly varying performances of the used HFPPs [31]. An additional observation
742 for the Volta PP is that the induced PS does not reach a steady state but further increases with
743 illumination time (Figure 7a). This can be explained by a further increasing patch size R with
744 increased WF due to ESD of water by secondary electrons and electrons scattered to low spatial
745 frequencies in the specimen. The scattered electrons have a strongly reduced intensity compared
746 to the unscattered electrons yielding two or more different time constants.
747 In contrast to our experimental results, Brink et al. [2] claimed a positive charging of the in-

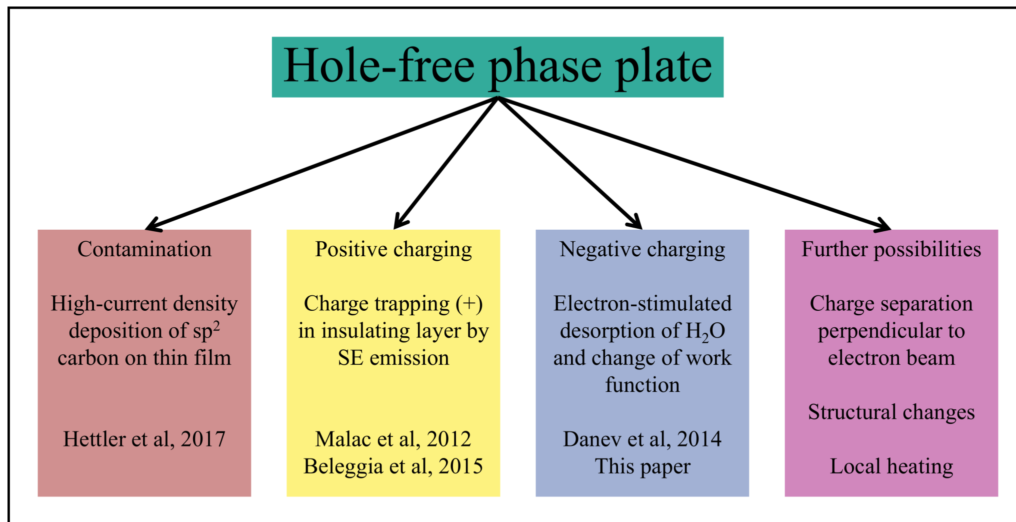

Figure 11: Graphical illustration of possible HFPP implementations.

748 vestigated aC thin film. The origin was supposed to come from highly localized positive charges
749 in a non-conductive layer of the thin film which could not be compensated by electrons from the
750 thin film itself due to a barrier. The experiments were conducted at the temperature of liquid
751 nitrogen suggesting a strongly reduced conductivity of the aC thin film and a thick layer of ad-
752 sorbed water on the surface. The experimental conditions differ largely from ours so that both
753 phenomena do not contradict each other.

754 The findings are also important for any phase-related (S)TEM imaging. The phase induced
755 by a thin film or a standard TEM sample is influenced by surface layers which we showed are
756 suspect to change upon focused electron-beam illumination. Phase measurements acquired by,
757 e.g., electron holography or focal-series reconstruction can be impaired by the described effects
758 if the investigated area has been previously illuminated inhomogeneously with a focused elec-
759 tron beam. The effect of an ESD-induced change of the work function and sample charging is
760 especially significant for SE measurements both in the SEM and TEM. The experimental results
761 show a strong influence of the WF on the number of detectable SEs (Figure 4) if a surface layer
762 is present. Although sample contamination is probably the most frequent artifact observed in
763 SEM, the change of the WF and a suppression of SE emission induced by ESD of surface layers
764 can additionally play a role in contrast formation in SEM imaging.

765 ## 5. Conclusions

766 We analyzed the charging of C thin films under focused electron-beam illumination in a
767 transmission electron microscope. Four different C thin films were studied by electron energy-
768 loss spectrosopy, hole-free phase plate (HFPP) imaging, detection of SEs and x-ray photoelectron
769 spectroscopy to identify the physical reason for the observed charging effects. Contamination
770 was avoided by suitable pretreatments as described in [16] which allows a clear separation of
771 contamination and charging. The following conclusions can be drawn:

ACCEPTED MANUSCRIPT

772 • The investigated C thin films exhibit an electrical conductivity which is sufficient to com-
773 pensate all charges created by illuminating high-energy electrons within the thin film if
774 they are kept at room temperature or above. If they are free from adsorbed surface layers,
775 the thin films do not charge.

776 • Negative charging is observed under intense focused electron-beam illumination if con-
777 tamination due to hydrocarbon molecules is avoided by appropriate pretreatments. Suit-
778 able measures are, e.g., UV cleaning, beam showering or heating which either immobilize
779 or remove the hydrocarbon molecules.

780 • Negative charging on contamination-free surfaces induces phase shifts with an amount less
781 than $\pi/2$. The physical reason for the negative charging is identified as electron-stimulated
782 desorption (ESD) of adsorbed water molecules in the illuminated area which results in a
783 local increase of the work function. The adsorbed water layer can be interpreted as a dipole
784 layer with the positive (H) end pointing to vacuum.

785 • A calculation of the electrostatic potential above a thin film with a circular patch at a
786 negative potential yields an expression for the relative phase shift between unscattered
787 electrons and electrons scattered to high spatial frequencies which is linearly dependent
788 on the radius R of the charged area and the amount of the work function change $e\delta V$.

789 • By comparison of experiment and calculation, the amount of work function change is
790 estimated to be $e\delta V$=0.4 eV in case of the single-layer graphene (SLG) thin film at room
791 temperature.

792 • Heating of the C thin films leads to desorption of all adsorbed molecules and to a van-
793 ishing negative charging. The temperature above which the surface layers are completely
794 desorbed depends on the structure of the thin film and was between 275 °C (PVD and
795 Thread aC) and 450 °C (SLG) for the analyzed C thin films.

796 • Strong structural differences between thin films denoted as 'aC' can occur which influence
797 the characteristics of the negative charging.

798 • The functionality of the HFPP [8] and the Volta phase plate [14] can be well explained
799 by the proposed model for the negative charging. The charging effect however depends
800 on numerous parameters, e.g. the amount of adsorbed water on, or the local structure of
801 the thin film, which are difficult to control. Depending on the operating parameters of
802 the HFPP, positive charge trapping [8] and carbon contamination [16] remain plausible
803 alternative explanations.

804 • Under certain conditions, ESD of hydrocarbon molecules and the deposition of hydrocar-
805 bon contamination layers can occur in parallel. The experimental results indicate that ESD
806 is taking place much faster than the deposition of contamination.

807 • The described model of charging could affect any phase-related technique in (scanning)
808 transmission electron microscopy and can influence the contrast of secondary electron
809 images.

ACCEPTED MANUSCRIPT

ACCEPTED MANUSCRIPT

Acknowledgments

S. Hettler acknowledges funding from the Karlsruhe House of Young Scientists (KHYS). The work performed at KIT was funded by the German Research Foundation (DFG). E. Kano acknowledges funding from JSPS KAKENHI Grant Number 15J04118. The support from Dr. M. Takeguchi and Dr. A. Hashimoto (NIMS, Japan) and the SLG sample offer from Dr. S. Sakai (QST, Japan) is gratefully acknowledged. The work at NINT was supported by the National Research Council of Canada. The ongoing support of Hitachi High Technologies (Naka, Japan) especially Dr. Y. Taniguchi and Hitachi High Technologies Canada (D. Hoyle and C. Soong) was crucial in developing a custom experimental setup of the Hitachi HF-3300. Collaboration with JEOL Ltd. and JEOL USA Inc. allowed us to pursue phase-plate development at NINT. In particular the help of Dr. M. Kawasaki (JEOL USA Inc.) and Dr. Y. Okura, Dr. S. Motoki, Dr. I. Ishikawa and Dr. Y. Konyuba (JEOL Ltd.) has been crucial in building the phase plate imaging at NINT. The fabrication of the EB aC thin film by Mike Marko (Wadsworth Centre, New York State University, Albany, NY, USA) and of the Thread aC thin film by Peter Hermann (LEM, Karlsruhe Institute of Technology, Karlsruhe, Germany) is acknowledged.

References

[1] R. Henderson, R. M. Glaeser, Quantitative analysis of image contrast in electron micrographs of beam-sensitive crystals, Ultramicroscopy 16 (1985) 139–150. doi:10.1016/0304-3991(85)90069-5.

[2] J. Brink, M. B. Sherman, J. Berriman, W. Chiu, Evaluation of charging on macromolecules in electron cryomicroscopy, Ultramicroscopy 72 (1998) 41–52. doi:10.1016/S0304-3991(97)00126-5.

[3] J. A. Berriman, P. B. Rosenthal, Paraxial charge compensator for electron cryomicroscopy, Ultramicroscopy 116 (2012) 106–114. doi:10.1016/j.ultramic.2012.03.006.

[4] K. Sader, M. Stopps, L. J. Calder, P. B. Rosenthal, Cryomicroscopy of radiation sensitive specimens on unmodified graphene sheets: reduction of electron-optical effects of charging, J Struct Biol 183 (3) (2013) 531–536. doi:10.1016/j.jsb.2013.04.014.

[5] C. J. Russo, L. A. Passmore, Progress towards an optimal specimen support for electron cryomicroscopy, Curr Opin Struc Biol 37 (2016) 81–89. doi:10.1016/j.sbi.2015.12.007.

[6] R. F. Egerton, P. Li, M. Malac, Radiation damage in the TEM and SEM, Micron 35 (6) (2004) 399–409. doi:10.1016/j.micron.2004.02.003.

[7] J. Cazaux, From the physics of secondary electron emission to image contrasts in scanning electron microscopy, J Electron Microsc 61 (5) (2012) 261–284. doi:10.1093/jmicro/dfs048.

[8] M. Malac, M. Beleggia, M. Kawasaki, P. Li, R. F. Egerton, Convenient contrast enhancement by a hole-free phase plate, Ultramicroscopy 118 (2012) 77–89. doi:10.1016/j.ultramic.2012.02.004.

[9] R. M. Glaeser, K. H. Downing, Specimen Charging on Thin Films with One Conducting Layer: Discussion of Physical Principles, Microsc Microanal 10 (06) (2004) 790–796. doi:10.1017/S1431927604040668.

[10] D. M. Larson, K. H. Downing, R. M. Glaeser, The surface of evaporated carbon films is an insulating, high-bandgap material, J Struct Biol 174 (2) (2011) 420–423. doi:10.1016/j.jsb.2011.02.005.

[11] R. Danev, K. Nagayama, Transmission electron microscopy with Zernike phase plate, Ultramicroscopy 88 (4) (2001) 243–252. doi:10.1016/S0304-3991(01)00088-2.

[12] K. Schultheiss, F. Pérez-Willard, B. Barton, D. Gerthsen, R. R. Schröder, Fabrication of a Boersch phase plate for phase contrast imaging in a transmission electron microscope, Rev Sci Instrum 77 (3) (2006) 033701. doi:10.1063/1.2179411.

[13] R. M. Glaeser, Invited review article: Methods for imaging weak-phase objects in electron microscopy, Rev Sci Instrum 84 (11) (2013) 111101. doi:10.1063/1.4830355.

[14] R. Danev, B. Buijsse, M. Khoshouei, J. M. Plitzko, W. Baumeister, Volta potential phase plate for in-focus phase contrast transmission electron microscopy, PNAS 111 (44) (2014) 15635–15640. doi:10.1073/pnas.1418377111.

[15] M. Malac, S. Hettler, M. Hayashida, M. Kawasaki, Y. O. Konyuba, Y. Okura, H. Iijima, I. Ishikawa, M. Beleggia, Computer simulations analysis for determining the polarity of charge generated by high energy electron irradiation of a thin film, Micron 100 (2017) 10–22. doi:10.1016/j.micron.2017.03.015.

860 [16] S. Hettler, M. Dries, P. Hermann, M. Obermair, D. Gerthsen, M. Malac, Carbon contamination in scanning
861 transmission electron microscopy and its impact on phase-plate applications, Micron 96 (2017) 38–47. doi:
862 10.1016/j.micron.2017.02.002.
863 [17] M. Bergen, Malac, M.,McLeod, R. A., D. Hoyle, Y. Taniguchi, Y. Yaguchi, J. Chen, T. Yotsuji, Centralized In-
864 strument Control for a TEM Laboratory, Microsc Microanal 19 (Suppl 2) (2013) 1394–1395. doi:10.1017/
865 S1431927613008969.
866 [18] R. F. Egerton, Electron energy-loss spectroscopy in the electron microscope, 3rd Edition, The language of science,
867 Springer, New York, 2011.
868 [19] L. Reimer, H. Kohl, Transmission electron microscopy: Physics of image formation, 5th Edition, Vol. 36 of
869 Springer series in optical sciences, Springer, New York, NY, 2009.
870 [20] S. Hettler, J. Wagner, M. Dries, M. Oster, C. Wacker, R. R. Schröder, D. Gerthsen, On the role of inelastic scat-
871 tering in phase-plate transmission electron microscopy, Ultramicroscopy 155 (2015) 27–41. doi:10.1016/j.
872 ultramic.2015.04.001.
873 [21] E. Kano, M. Takeguchi, J.-i. Fujita, A. Hashimoto, Direct observation of Pt-terminating carbyne on graphene,
874 Carbon 80 (2014) 382–386. doi:10.1016/j.carbon.2014.08.077.
875 [22] C. Soong, P. Woo, D. Hoyle, Contamination Cleaning of TEM/SEM Samples with the ZONE Cleaner, Micros
876 Today 20 (06) (2012) 44–48. doi:10.1017/S1551929512000752.
877 [23] S. J. Pennycook, P. D. Nellist, Scanning transmission electron microscopy: Imaging and analysis, Springer, New
878 York, 2011.
879 [24] P. Wachsmuth, R. Hambach, G. Benner, U. Kaiser, Plasmon bands in multilayer graphene, Phys. Rev. B 90 (23)
880 (2014) 235434. doi:10.1103/PhysRevB.90.235434.
881 [25] E. Völkl, L. F. Allard, D. C. Joy, Introduction to electron holography, Springer, New York, 1999.
882 [26] M. Wanner, D. Bach, D. Gerthsen, R. Werner, B. Tesche, Electron holography of thin amorphous carbon films: mea-
883 surement of the mean inner potential and a thickness-independent phase shift, Ultramicroscopy 106 (4-5) (2006)
884 341–345. doi:10.1016/j.ultramic.2005.10.004.
885 [27] M. Dries, S. Hettler, T. Schulze, W. Send, E. Müller, R. Schneider, D. Gerthsen, Y. Luo, K. Samwer, Thin-Film
886 Phase Plates for Transmission Electron Microscopy Fabricated from Metallic Glasses, Microsc Microanal 22 (5)
887 (2016) 955–963. doi:10.1017/S143192761601165X.
888 [28] F. Sette, G. K. Wertheim, Y. Ma, G. Meigs, Lifetime and screening of the C 1s photoemission in graphite, Phys
889 Rev B 41 (14) (1990) 9766–9770. doi:10.1103/PhysRevB.41.9766.
890 [29] S. T. Jackson, G. R. Nuzzo, Determining hybridization differences for amorphous carbon from the XPS C1s enve-
891 lope, Appl surf sci 90 (1995) 195–203. doi:10.1016/0169-4332(95)00079-8.
892 [30] H. Estrade-Szwarckopf, XPS photoemission in carbonaceous materials: A "defect" peak beside the graphitic asym-
893 metric peak, Carbon 42 (8-9) (2004) 1713–1721. doi:10.1016/j.carbon.2004.03.005.
894 [31] M. Marko, C. Hsieh, E. Leith, D. Mastronarde, S. Motoki, Practical Experience with Hole-Free Phase Plates for
895 Cryo Electron Microscopy, Microsc Microanal 22 (6) (2016) 1316–1328. doi:10.1017/S143192761601196X.
896 [32] J. J. Hren, Specimen contamination in analytical electron microscopy: Sources and solutions, Ultramicroscopy 3
897 (1979) 375–380. doi:10.1016/S0304-3991(78)80057-6.
898 [33] E. M. Williams, J. L. de Segovia, Electron stimulated desorption of ions from surfaces: Techniques, methodology
899 and some recent findings with water at metals and semiconductors, Vacuum 39 (7/8) (1989) 633–642. doi:
900 10.1016/0042-207X(89)90006-7.
901 [34] R. D. Ramsier, J. T. Yates, Electron-stimulated desorption: principles and applications, Surf Sci Rep 12 (1991)
902 243–378. doi:10.1016/0167-5729(91)90013-N.
903 [35] W. F. van Dorp, C. W. Hagen, A critical literature review of focused electron beam induced deposition, J Appl Phys
904 104 (8) (2008) 081301. doi:10.1063/1.2977587.
905 [36] I. Utke, P. Hoffmann, J. Melngailis, Gas-assisted focused electron beam and ion beam processing and fabrication,
906 J. Vac. Sci. Technol. B 26 (4) (2008) 1197. doi:10.1116/1.2955728.
907 [37] W. F. van Dorp, T. W. Hansen, J. B. Wagner, J. T. M. De Hosson, The role of electron-stimulated desorption in
908 focused electron beam induced deposition, Beilstein J Nanotechnol 4 (2013) 474–480. doi:10.3762/bjnano.
909 4.56.
910 [38] R. L. Wells, T. J. Fort, Adsorption of water on clean gold by measurement of work function changes, Surf Sci 32
911 (1972) 554–560. doi:10.1016/0039-6028(72)90182-3.
912 [39] J. M. Heras, L. Viscido, Work function changes upon water contamination of metal surfaces, Appl surf sci 4 (1980)
913 238–241.
914 [40] P. A. Thiel, T. E. Madey, The interaction of water with solid surfaces: Fundamental aspects, Surf Sci Rep 7 (1987)
915 211–385. doi:10.1016/0167-5729(87)90001-X.
916 [41] J. M. Heras, G. Estiú, L. Viscido, The interaction of water with clean palladium films: A thermal desorption and
917 work function study, Appl surf sci 108 (455-464). doi:10.1016/S0169-4332(96)00686-1.
918 [42] M. A. Henderson, The interaction of water with solid surfaces: fundamental aspects revisited, Surf Sci Rep 46

ACCEPTED MANUSCRIPT

ACCEPTED MANUSCRIPT

919 (2002) 1–308. doi:10.1016/S0167-5729(01)00020-6.
920 [43] J. M. Heras, G. Estiú, L. Viscido, Annealing behaviour of clean and oxygen covered polycrystalline Palla-
921 dium films: a work function and electrical resistance study, Thin Solid Films 188 (1990) 165–172. doi:
922 10.1016/0040-6090(90)90202-O.
923 [44] M. Beleggia, M. Malac, T. Rowan, R. F. Egerton, M. Kawasaki, Y. Okura, R. A. McLeod, Electron beam-
924 induced charging and modifications of thin films, Microsc Microanal 21 (S3) (2015) 1385–1388. doi:10.1017/
925 S1431927615007710.

ACCEPTED MANUSCRIPT